Journal of Geophysical Research: Solid Earth

RESEARCH ARTICLE
10.1002/2015JB012195

Magnitudes and moment-duration scaling of low-frequency earthquakes beneath southern Vancouver Island

M. G. Bostock[1], A. M. Thomas[2], G. Savard[1], L. Chuang[1], and A. M. Rubin[3]

[1]Department of Earth, Ocean and Atmospheric, University of British Columbia, Vancouver, British Columbia, Canada, [2]Department of Geophysics, Stanford University, Stanford, California, USA, [3]Department of Geosciences, Princeton University, Princeton, New Jersey, USA

Key Points:
- Moment magnitudes estimated for almost 270,000 LFE detections below southern Vancouver Island
- Moment variation in space, time, and frequency is examined
- LFE moment-duration scaling is distinct from both slow earthquakes and regular seismicity

Correspondence to:
M. G. Bostock,
bostock@eos.ubc.ca

Citation:
Bostock, M. G., A. M. Thomas, G. Savard, L. Chuang, and A. M. Rubin (2015), Magnitudes and moment-duration scaling of low-frequency earthquakes beneath southern Vancouver Island, *J. Geophys. Res. Solid Earth*, *120*, doi:10.1002/2015JB012195.

Received 11 MAY 2015
Accepted 13 AUG 2015
Accepted article online 19 AUG 2015

Abstract We employ 130 low-frequency earthquake (LFE) templates representing tremor sources on the plate boundary below southern Vancouver Island to examine LFE magnitudes. Each template is assembled from hundreds to thousands of individual LFEs, representing over 269,000 independent detections from major episodic-tremor-and-slip (ETS) events between 2003 and 2013. Template displacement waveforms for direct *P* and *S* waves at near epicentral distances are remarkably simple at many stations, approaching the zero-phase, single pulse expected for a point dislocation source in a homogeneous medium. High spatiotemporal precision of template match-filtered detections facilitates precise alignment of individual LFE detections and analysis of waveforms. Upon correction for 1-D geometrical spreading, attenuation, free surface magnification and radiation pattern, we solve a large, sparse linear system for 3-D path corrections and LFE magnitudes for all detections corresponding to a single-ETS template. The spatiotemporal distribution of magnitudes indicates that typically half the total moment release occurs within the first 12–24 h of LFE activity during an ETS episode when tidal sensitivity is low. The remainder is released in bursts over several days, particularly as spatially extensive rapid tremor reversals (RTRs), during which tidal sensitivity is high. RTRs are characterized by large-magnitude LFEs and are most strongly expressed in the updip portions of the ETS transition zone and less organized at downdip levels. LFE magnitude-frequency relations are better described by power law than exponential distributions although they exhibit very high *b* values $\geq\sim 5$. We examine LFE moment-duration scaling by generating templates using detections for limiting magnitude ranges ($M_W < 1.5$, $M_W \geq 2.0$). LFE duration displays a weaker dependence upon moment than expected for self-similarity, suggesting that LFE asperities are limited in fault dimension and that moment variation is dominated by slip. This behavior implies that LFEs exhibit a scaling distinct from both large-scale slow earthquakes and regular seismicity.

1. Introduction

The discovery of tectonic tremor in southwest Japan [*Obara*, 2002] and its subsequent association with slow slip in Cascadia [*Dragert et al.*, 2001; *Rogers and Dragert*, 2003] has initiated a new field of earthquake study and led to important insights into deformation processes at plate boundaries. The tremor component of tremor-and-slip involves motions with dominant frequencies in the 1–10 Hz band that are readily measured by short-period and broadband network seismometers. Consequently, where GPS recordings are not available or when signal-to-noise levels of GPS recordings are low, tremor is often used as a proxy for the slow slip it is inferred to accompany.

Much attention has been directed toward studies of tremor phase, for example, in location [*Obara*, 2002; *Kao et al.*, 2005; *Wech and Creager*, 2011; *Ide*, 2010], association of tremor with swarms of repeating low-frequency earthquakes (LFEs) [*Shelly et al.*, 2006], characterization of primary and secondary tremor fronts [*Ghosh et al.*, 2012; *Houston et al.*, 2011; *Rubin and Armbruster*, 2013; *Peng et al.*, 2015], modulation of tremor and LFE activity by surface waves and tides [*Rubinstein et al.*, 2008; *Shelly et al.*, 2007], spatial variations in tremor recurrence intervals [*Brudzinski and Allen*, 2007; *Wech and Creager*, 2011], tremor migration patterns [*Obara and Sekine*, 2009; *Wech and Bartlow*, 2014], and seismic moment proxies for slow slip based on tremor cumulative duration [*Aguiar et al.*, 2009].

Rather less effort has been expended in the direct characterization of tremor and LFE amplitudes. *Watanabe et al.* [2007] examined the duration of reduced displacement above a fixed threshold in tremor bursts as a proxy for magnitude in southwest Japan. They argued that the duration-amplitude distribution of tremor best conforms to an exponential model, suggesting it is governed by a scale-bound source process. *Kao et al.* [2010] calibrated maximum amplitudes of short (5 s) tremor bursts with regional seismicity catalogs for Vancouver Island and inferred magnitudes of tremor bursts to fall between $M_W \sim 1.0-1.7$. *Sweet et al.* [2014] also utilized moment calibration with local earthquakes to analyze the behavior of LFEs associated with a single family below northern Puget Sound. They found that cumulative moment correlates with time to next swarm, suggesting that LFE swarms are time predictable. *Wech et al.* [2010] employed the tremor duration-moment scaling of *Aguiar et al.* [2009] to argue that the slow-slip magnitude-frequency distribution is similar to regular earthquakes with a *b* value of 1. Other studies have examined tremor amplitude dependence upon distance to place constraints on the attenuation of seismic waves in subduction zones, noting that the tremor frequency band (1–10 Hz) is of interest for ground motion prediction. Tremor data in northern Cascadia were exploited by *Baltay and Beroza* [2013] to quantify peak ground acceleration and velocity and develop an anelastic attenuation parameter for that region. *Yabe et al.* [2014] extended this work to Nankai, Mexico, and Chile. They demonstrated that lower crust in the overriding plate is more attenuating than upper crust and is underlain by a highly attenuating, subducted oceanic crust.

In this study, we exploit high signal-to-noise ratio (SNR) LFE templates to estimate individual LFE detection magnitudes from 10 episodic-tremor-and-slip (ETS) episodes recorded on southern Vancouver Island. Unlike the studies of *Kao et al.* [2010] and *Sweet et al.* [2014], we avoid calibration by local regular earthquakes, but rather exploit the spatiotemporal precision of LFE templates to measure moment directly from first arrival *P* and *S* waveforms of individual detections.

2. Data

We employ a catalog of LFE detections from southern Vancouver Island assembled from 10 major ETS episodes between 2003 and 2013. This catalog comprises those templates from *Bostock et al.* [2012] and *Royer and Bostock* [2013], as well as new additions for a total of 130 distinct source regions on the plate boundary. The largest (and presumably most complete) contributions come from the years 2003–2005 during which stations from the POLARIS-BC array were operational [*Nicholson et al.*, 2005]; see Figure 1. Tremor data from these episodes enabled the construction of an initial set of high-SNR LFE templates for network-matched filtering that were applied to data from subsequent episodes (2007–2013) using initial subsets of common stations. The catalog employed in the present study has been culled such that only the detection with the strongest correlation in any given 4 s interval (approximate maximum duration of the *S* wave coda) is retained, resulting in a total of 269,586 detections across all years.

LFE detections from template-matched filtering hold a distinct advantage for the present purpose, namely, that of high spatiotemporal resolution. This property permits us to extract precise windows, defined from the templates, containing the desired direct wave signals from individual detections. Moreover, the practically identical source-receiver paths for repeating LFEs allow amplitude bias by unmodeled structure to be more effectively removed. As argued by *Royer and Bostock* [2013], LFE templates can be regarded as empirical, band-limited Green's functions. For subsets of stations at short epicentral distances, templates reveal particularly simple waveforms: dipolar pulses in particle velocity and single pulses in particle displacement; hence, the direct wave is easily identified and consistent across these stations. This property has been exploited in cross-channel-correlation detection schemes [*Rubin and Armbruster*, 2013; *Armbruster et al.*, 2014; *Peng et al.*, 2015; *Savard and Bostock*, 2015] that resolve fine-scale behavior of tremor fronts. It also facilitates analysis of LFE magnitudes by enabling a precise isolation of waveforms associated with the distinct, direct *P* and *S* wave arrivals. More specifically, our data windowing approach incorporates the following elements. For each family of detections corresponding to a given LFE template

1. Template waveforms, filtered between 1–8 Hz and 6 s in length, for *P* (Z component) and *S* (N, E components) are initially aligned using predicted times from the 1-D model used for routine earthquake location by the Geological Survey of Canada.
2. Fine alignment is achieved through an approach [*Bungum and Husebye*, 1971] wherein individual template waveforms are iteratively shifted using correlation with the composite waveform stack from a previous iteration until convergence is achieved (note, *P* and *S* waves are treated independently).

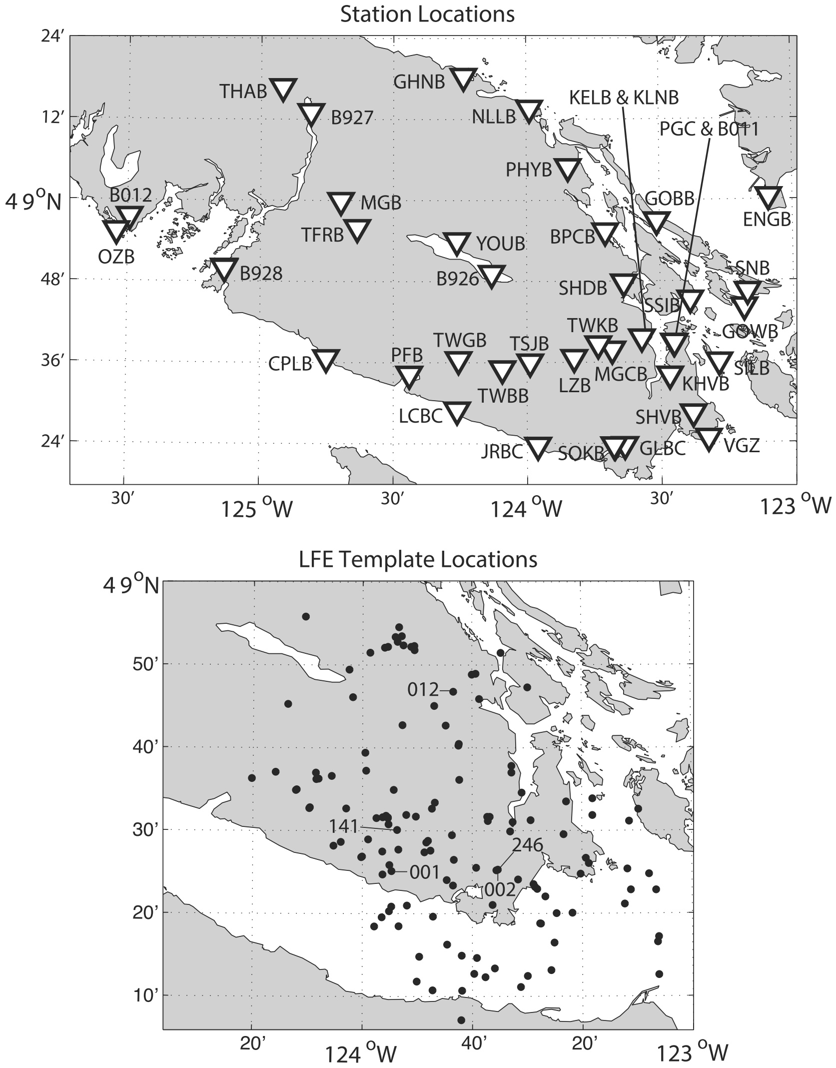

Figure 1. (top) Map of stations and (bottom) LFE template locations employed in this study. Templates referred to in text are identified by number in Figure 1 (bottom).

3. A 2.0 s duration "detection" window (including 0.25 s half-cosine taper at either edge) is defined about the center of the maximum of the envelope corresponding to the final template waveform stack.
4. A particular station and channel is admitted for further analysis if (i) the correlation coefficient of the template channel with the final template stack exceeds 0.4 and (ii) the energy within the detection window exceeds 70% of that in the total (6 s long) channel trace. These conditions admit waveforms that are dominated by a direct wave arrival with minimal interference from, e.g., triplicated, converted, and other secondary phases. Figure 2 displays those waveforms for template 001 that satisfied both criteria;
5. Using the time shifts determined in 1 – 3 and the channels selected in 4, we extract corresponding 2.0 s data windows from individual LFE detections for available channels (a template is constructed from all possible station/channels that have recorded signal in any one of the total 10 ETS episodes; however, only a subset of these station/channels are available for any given episode due, e.g., to temporary network deployments). If the channel waveform for an individual detection exhibits a correlation coefficient with the corresponding template channel greater than 0.25, we use it in the magnitude calculation. Figure 3 displays waveforms admitted for magnitude calculation (nonzero blue) traces based on available channels for an LFE on 3 March 2003 at 01:14:36 UTC.

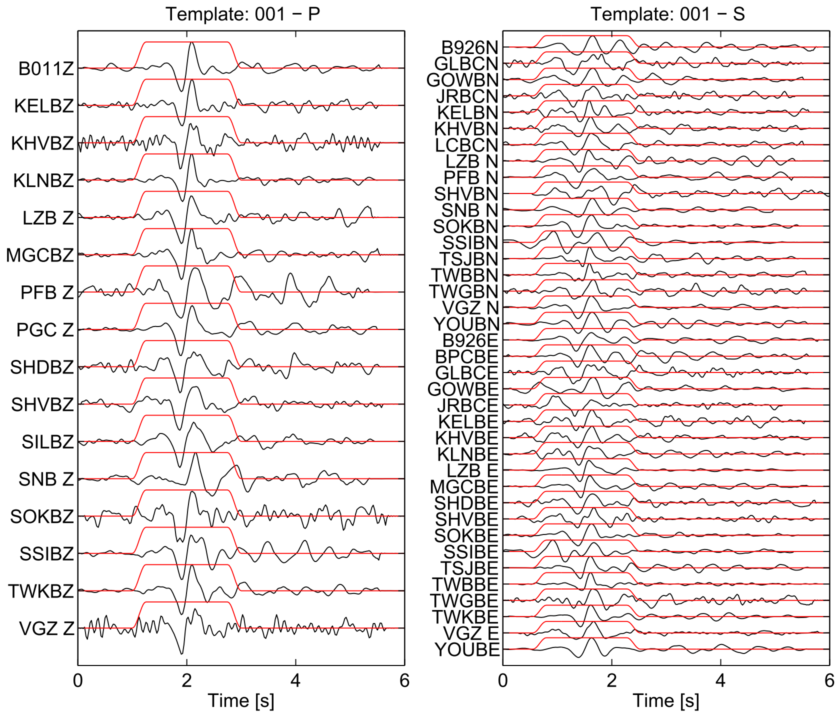

Figure 2. Example particle-velocity template waveforms for family 001 used in magnitude calculations for individual detections belonging to that family. These waveforms display isolated direct wave pulses for (left) *P* waves and (right) *S* waves. Red mask depicts 2.0 s long detection window used to isolate direct wave for individual detections (when the correlation coefficient between template and detection waveform exceeds 0.25; see Figure 3). Note that *P* wave polarities have been normalized based on expected radiation pattern from focal mechanism determined by *Royer and Bostock* [2013].

3. Methodology

We represent the ith component, displacement seismogram of a direct P or S wave, $u_i(\mathbf{x},t)$ recorded at a surface location $\mathbf{x}$ from a low-frequency earthquake at $\mathbf{x}'$ in the ray approximation [e.g., *Chapman*, 2004] as

$$u_i(\mathbf{x},t) = A(\mathbf{x},\mathbf{x}')\,E(\mathbf{x},\mathbf{x}')\,F_{ij}(\mathbf{x},\mathbf{x}')\,R_j(\mathbf{x},\mathbf{x}')\,\dot{M}_0(t-\tau(\mathbf{x},\mathbf{x}')), \tag{1}$$

where $\dot{M}_0(t-\tau(\mathbf{x},\mathbf{x}'))$ is the scalar moment rate, $\tau(\mathbf{x},\mathbf{x}')$ is the P or S wave traveltime function between source at $\mathbf{x}'$ and the surface receiver at $\mathbf{x}$, $R_j(\mathbf{x},\mathbf{x}')$ describes the radiation pattern of the source, $F_{ij}(\mathbf{x},\mathbf{x}')$ accounts for amplification at the free surface, $E(\mathbf{x},\mathbf{x}')$ describes intrinsic attenuation and $A(\mathbf{x},\mathbf{x}')$ incorporates scaling by material properties, transmission coefficients, and geometrical spreading. More specifically,

$$R_j(\mathbf{x},\mathbf{x}') = \hat{s}_j(\mathbf{x})\,\hat{s}_k(\mathbf{x}')\,\hat{p}_l(\mathbf{x}')\,\hat{M}_{kl}, \tag{2}$$

where $\hat{M}_{kl}$ represents the unit moment tensor and $\hat{s}_i, \hat{p}_i$ are unit polarization and slowness vectors, respectively. The factor $A(\mathbf{x},\mathbf{x}')$ is defined as

$$A(\mathbf{x},\mathbf{x}') = \frac{\prod_i \mathbf{T}_i}{4\pi\,V^2(\mathbf{x}')\sqrt{\rho(\mathbf{x})\,\rho(\mathbf{x}')\,V(\mathbf{x})\,V(\mathbf{x}')\,X(\mathbf{x},\mathbf{x}')}}, \tag{3}$$

where we assume that no caustics are encountered en route to the surface, T_i represent transmission coefficients at discontinuous boundaries in material properties between the source depth and the surface, density and P or S velocity are denoted by ρ and V, respectively, and $X^{1/2}(\mathbf{x},\mathbf{x}')$ is the geometrical spreading function that solves the transport equation. We will further approximate the aforementioned quantities by assuming that propagation takes place in the laterally homogeneous, isotropic medium defined in Table 1, except that attenuation is taken to be a simple function of hypocentral distance

$$E(\mathbf{x}) = \mathrm{e}^{-C|\mathbf{x}-\mathbf{x}'|}, \tag{4}$$

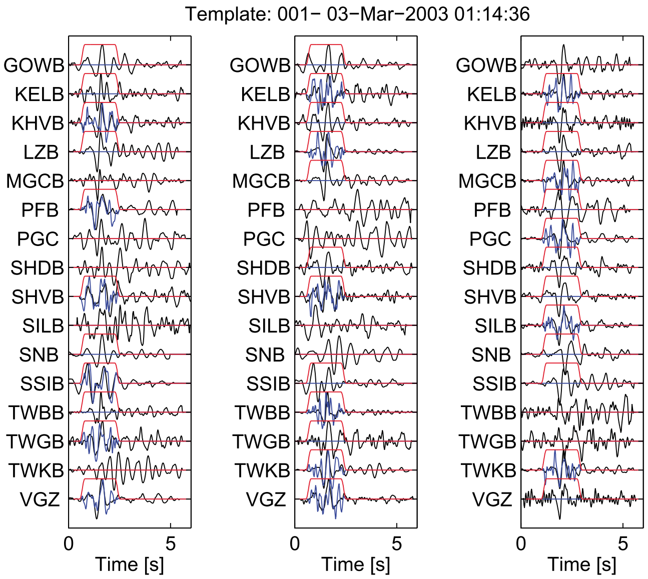

Figure 3. Detection (particle velocity) waveforms (nonzero blue traces) admitted for magnitude calculation corresponding to an LFE that occurred on 3 March 2003 at 01:14:36. Detection waveforms must pass two criteria: (i) their corresponding template waveform (black traces) must exhibit a simple direct arrival based on waveform similarity with other template waveforms (see text for details) and (ii) the detection waveform must possess a correlation coefficient greater than 0.25 with its respective template waveform. Red traces denote temporal mask used to isolate detection waveforms; zero masks denote station-channels that failed to meet criterion (i). Zeroed blue traces correspond to detection waveforms that did not meet criterion (ii). (left and middle) *S* wave channels on north and east components, respectively; (right) *P* waves on vertical component.

using a nominal value of $C_S = 0.005\ \mathrm{km}^{-1}$ ($Q_S \sim 650$) based on the tremor studies of *Baltay and Beroza* [2013] and *Yabe et al.* [2014] for *S* waves and assume $Q_P = Q_S$ (or $C_P = 0.0029\ \mathrm{km}^{-1}$) for *P* waves. The unit moment tensor $\hat{M}_{kl}$ is represented by the average double couple mechanism for LFE templates on southern Vancouver Island reported by *Royer and Bostock* [2013]. This mechanism is consistent with shallow thrusting in a northeasterly direction.

Following standard practice by integrating both sides of (1) with respect to time and rearranging factors, we arrive at an expression for the scalar moment M_0 from a single-channel (station and component) *P* or *S* wave seismogram $u_j(\mathbf{x}, t)$ as

$$M_0 = \frac{\int \mathrm{d}t\, \acute{u}_j(\mathbf{x}, t)}{A(\mathbf{x}, \mathbf{x}')\, E(\mathbf{x}, \mathbf{x}')\, R_j(\mathbf{x}, \mathbf{x}')}, \tag{5}$$

(no summation in *j*) where the integration can be performed in the frequency domain by measuring the spectral low-frequency asymptote. In practice, we employ the maximum spectral value between 1 and 1.5 Hz. An estimate of the upgoing wavefield, $\acute{u}_i(\mathbf{x}, t)$, is recovered from $u_i(\mathbf{x}, t)$ by removing the amplification of a planar free surface, as expressed in vector notation (*i.e.*, $F_{ij} \rightarrow \mathbf{F}$) as

$$\acute{\mathbf{u}} = \mathbf{F}^{-1}\mathbf{u} = \mathbf{B}^T\mathbf{W}^{-1}\mathbf{B}\mathbf{u}. \tag{6}$$

This operation entails an application of the inverse free surface transfer operator $\mathbf{W}^{-1}$ [*Kennett*, 1991], sandwiched between rotations into ($\mathbf{B}$) and out of ($\mathbf{B}^T$) the horizontal radial/transverse coordinate frame defined by the source-receiver geometry.

Table 1. Velocity Model Used to Account for Wave Propagation[a]

Layer Number	Depth to Top (km)	V_P (km/s)
1	0.0	5.0
2	1.0	6.0
3	6.0	6.7
4	30.0	7.1
5	45.0	7.75

[a] A Poisson solid is assumed and Birch's Law is employed for density.

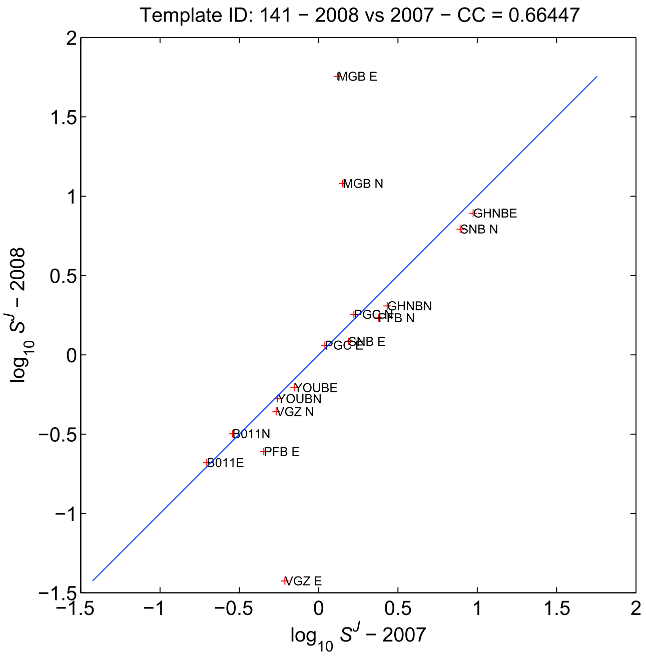

Figure 4. Path corrections expressed in $\log_{10}$ for template 141 at stations common to ETS episodes in 2007 and 2008 from a preliminary inversion using only S waves. Note that both horizontal components at station MGB and the east component of station VGZ differ significantly between the 2 years and have been withdrawn from subsequent inversions for detections in 2007. All templates for these two episodes display similar patterns for these three channels. A line with slope 1 is shown in blue.

The measurement in (5) made for multiple channels is likely to vary significantly due to inadequacies in the modeling, for example, the assumption of a laterally homogeneous and isotropic overriding North American plate. Significant lateral heterogeneity has been documented in regional tomographic studies [e.g., *Ramachandran et al.*, 2005; *Zhao et al.*, 2001], whereas crustal anisotropy has been characterized in some detail by, e.g., recent studies of *Balfour et al.* [2011] and *Matharu et al.* [2014]. We can exploit the multiplicity of detections for a given LFE family to mitigate these contaminating influences. All such detections share virtually the same receiver path and so errors due to unmodeled structure will be common. Denoting the estimate of M_0 determined through (5) for the Ith detection using the Jth channel as M_0^{IJ}, we relate this estimate to the "true" moment M_0^I through a multiplicative "path" correction S^J for the Jth station channel that accounts for any source-to-receiver propagation effects not adequately represented by our isotropic, 1-D model. Expressed in logarithms and following, e.g., *Andrews* [1986], we have

$$\log M_0^{IJ} = \log M_0^I + \log S^J. \tag{7}$$

Accordingly, each family of detections results in a large, overdetermined but singular, sparse system of equations that can be resolved through the inclusion of one additional constraint. We assume that inadequacies in the forward modeling (including representation of local site structure) average out over many stations, and so set

$$\sum_J \log S^J = 0. \tag{8}$$

Before solving the overdetermined system represented by (7) and (8), we weight each equation in (7) by the inverse of an estimate of relative error $\delta d^{IJ}/d^{IJ}$ in the corresponding datum as determined from the correlation coefficient c^{IJ} between the detection channel waveform and the associated template waveform (over windows defined by red masks in Figure 2). This estimate is

$$\frac{\delta d^{IJ}}{d^{IJ}} = \frac{\sqrt{1-(c^{IJ})^2}}{c^{IJ}}, \tag{9}$$

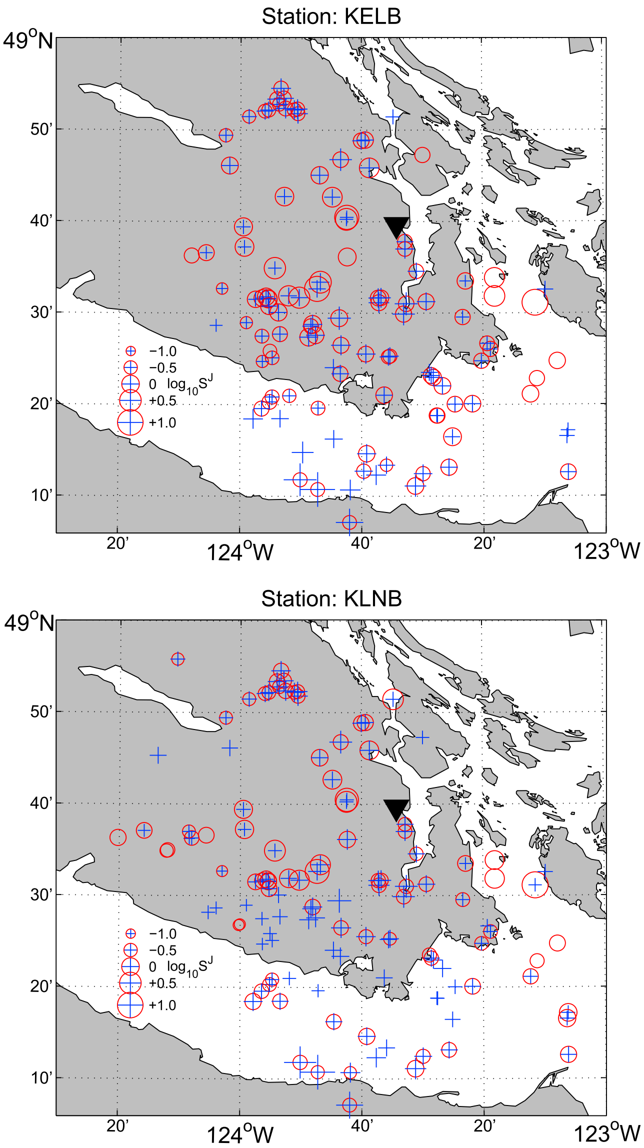

Figure 5. Examples of path corrections S^J for north (red circles) and east (blue plusses) components as a function of LFE template location for stations (top) KELB and (bottom) KLNB. Note these two stations were separated by a few tens of meters and were operational in separate ETS episodes (locations shown as inverted black triangles).

and is based on the assumption that the template waveform is error free and that noise in the detection waveform is uncorrelated with the true signal (only detection waveforms exhibiting $c^{IJ} \geq 0.25$ are admitted to the system). We proceed to solve the system using iteratively reweighted least squares [e.g., *Scales and Gersztenkorn*, 1988] to approximate a minimization of the L1 residual norm.

4. Results

4.1. Path Corrections

In addition to the single simultaneous inversion for LFE magnitudes M_0^I and station-channel path corrections S^J across all ETS episodes between 2003 and 2013 that we discuss in this and the following sections, we also performed preliminary inversions for episodes in single years to compare the consistency of S^J at stations common to pairs of episodes. This exercise revealed a high degree of consistency across a large majority of stations, but also a few discrepancies. For example, the S^J for north and east components at station MGB and the east component of VGZ are clearly different between templates in 2007 versus other episodes (see Figure 4). Hence, we have removed these stations from subsequent inversions of 2007 detections. We note a similar

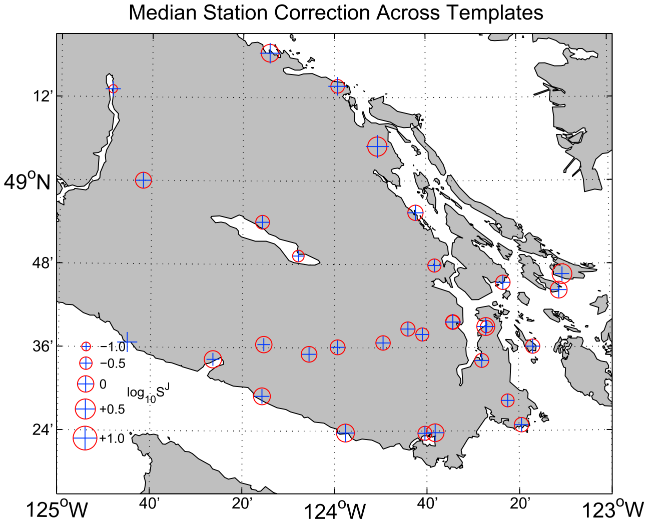

Figure 6. Median values of S^J for each station computed across all templates and plotted at station location.

change in the north component of B927 between the 2008 and 2009 ETS episodes and have restricted use of data therefrom to after 2008. Stations SHDB and SHVB were temporary network sites (re)occupied only within ETS episodes between 2003 and 2007, with contrasting S^J in different years [*Kao et al.*, 2005]. This observation may signal that either slightly different sites with variable coupling were chosen in different years or that different instruments were employed (but not registered in associated instrument response files). We restricted use of these two stations to 2003 alone. With the preceding adjustments made, correlation coefficients for path corrections $\log S^J$ at common stations for pairs of ETS episodes are typically well above 0.9.

Path corrections plotted as a function of LFE template location display systematic variations in space. Figure 5 includes path correction maps plotted for two stations, KELB and KLNB, that occupied almost the same location (separated by several tens of meters) for episodes in 2003 (KELB) and 2004–2005 (KLNB). Thus, they share no detections and are represented by independent templates that admitted different channel combinations to the inversions. Path corrections S^J are similar for both stations for those components and template locations that are shared. N and E components tend to covary closely and vary relatively smoothly over the region with a tendency for small magnitudes below the Strait of Juan de Fuca and larger magnitudes to the west and southwest within Vancouver Island. Other stations show comparable scales of variation. Figure 6 displays the median path correction for individual stations plotted at the respective station location. These values range between −1.0 and 0.6 $\log_{10}$ units. Figure 7 shows a histogram of all path correction terms that displays a distribution skewed to larger values as previously reported by *Yabe et al.* [2014] for tremor data.

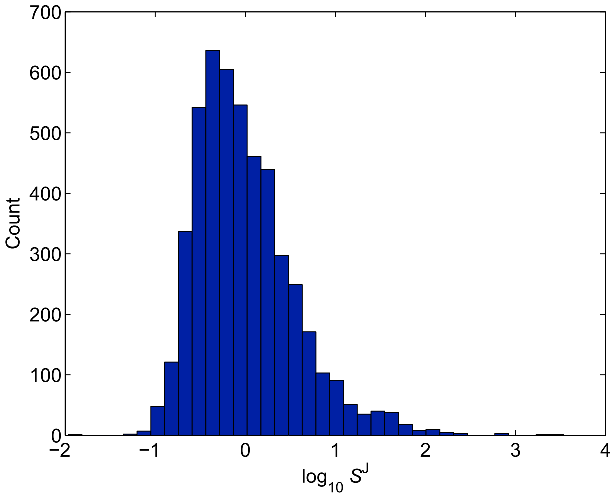

Figure 7. Histogram of path corrections S^J for all channels and templates. Note skew to larger values.

4.2. Magnitude-Frequency Relations

We now proceed to consider the LFE magnitude-frequency distribution using maximum likelihood estimation [e.g., *Clauset et al.*, 2009; *Alstott et al.*, 2014]. We will model the moment data set with a power law probability density in the form

$$p(M_0) = \frac{\beta - 1}{\check{M}_0}\left(\frac{M_0}{\check{M}_0}\right)^{-\beta}, \qquad (10)$$

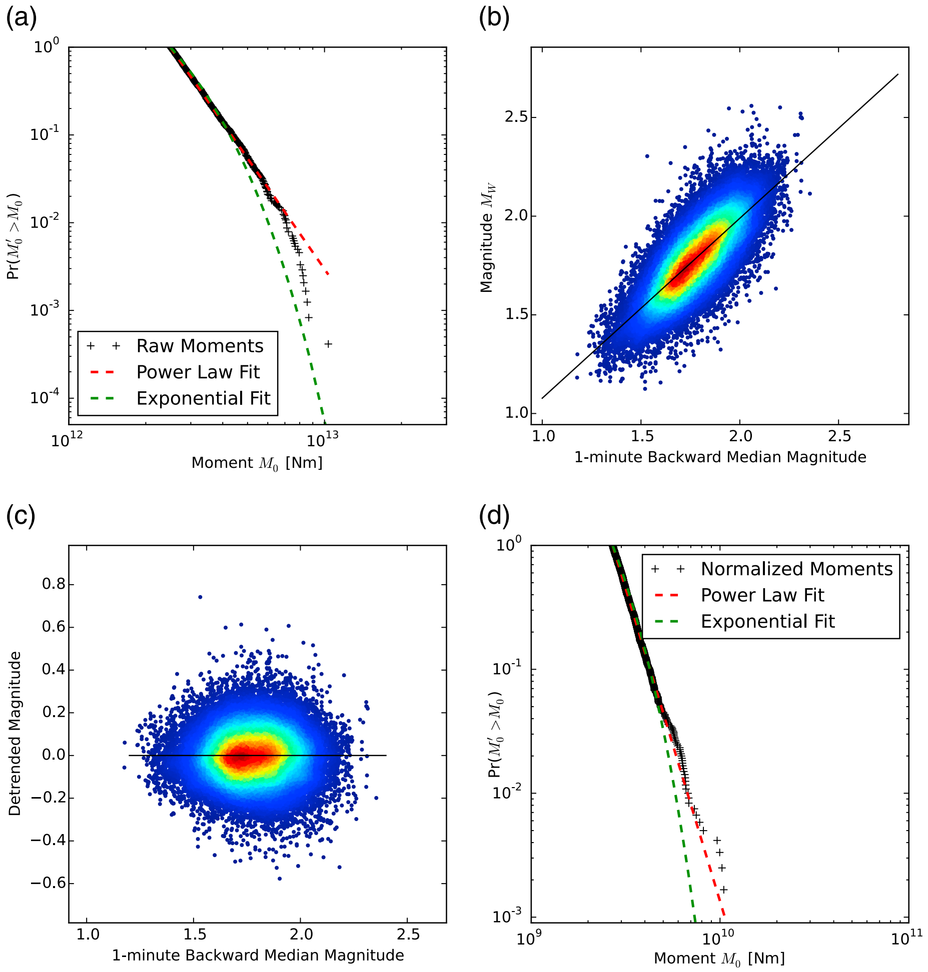

Figure 8. LFE magnitude-frequency relations. (a) The complementary cumulative probability distribution (CCPD) for moment measurements (black crosses) above minimum moment $M_0 = 2.49 \times 10^{12}$. Red dashed line shows maximum likelihood estimate for best power law fit with exponent $\beta = 5.19$ (or equivalently b value ≈ 6.3). Green dashed line indicates best exponential distribution for same minimum moment. (b) A density scatterplot of moment magnitude versus median magnitude in 1 min preceding respective detection for all detections with at least 10 detections in the preceding minute (total 37,348). Note strong linear correlation. (c) The same population but with removal of linear trend. (d) CCPD of moments corresponding to detrended magnitudes, along with maximum likelihood power law and exponential fits. Maximum likelihood fits are made for data with normalized moment $\geq 2.7 \times 10^9$ N m, yielding $\beta = 6.05$ (b value = 7.58).

and corresponding complementary cumulative distribution function

$$P(M_0) = \Pr(M_0' > M_0) = \int_{M_0}^{\infty} p(M_0')\mathrm{d}M_0' = \left(\frac{M_0}{\check{M}_0}\right)^{-\beta+1} . \tag{11}$$

Here $\check{M}_0$ represents the lower moment limit over which the power law fit holds and β is the exponent that best models the data. The quantities $p(M_0)$, $P(M_0)$ are normalized incremental and cumulative LFE moment distributions, respectively. The maximum likelihood estimate for the exponent of the raw moment catalog is $\beta = 5.19 \pm 0.09$ determined for an optimal $\check{M}_0 = 2.49 \times 10^{12}$ N m ($\check{M}_W = 2.20$) as shown in Figure 8a, where $P(M_0)$ is displayed. Lower values of $\check{M}_W$ result in slightly smaller β but diminish the fit based on a Kolmogorov-Smirnov log likelihood ratio test. The dashed red line represents the power law fit, whereas the dashed green line displays the best exponential fit. The corresponding b value $b = 1.5\,(\beta - 1) \approx 6.3$ is much higher than that for typical earthquakes ($b \sim 1$) contrary to the results of *Kao et al.* [2010] for short-tremor bursts on Vancouver Island, but qualitatively consistent with the study of a single-template family in northern Washington by *Sweet et al.* [2014] who reported a b value of about 4. Unlike the latter study, the power law description yields a better fit to our results than an exponential distribution, at least over the upper moment range ($\geq \check{M}_0$) where the heavy tails of the former are best distinguished.

Our M_W estimates range between 1.0 and 2.61 and are therefore generally larger than values reported by *Kao et al.* [2010] and *Sweet et al.* [2014] that fall between 1–1.7 and 0.3–1.5, respectively. We suspect that lower values in both previous studies result from calibration with waveform amplitudes of local earthquakes that possess higher frequencies relative to LFEs of comparable magnitude. The upper limit of M_W near 2.6 (or $M_0 \approx 1.0 \times 10^{13}$ N m) appears to be well defined; any detections registered above $M_W \approx 2.61$ have proven to be false.

In Figure 8b, we plot the moment catalog against a proxy for background tremor level, specifically the median moment in a 1 min window preceding each individual detection, for all (37,348) detections with at least 10 prior detections in that window. The obvious correlation with slope close to 1 suggests that either the LFE magnitude-frequency relation or our detection thresholds (or both) are time varying and depend upon background tremor level. If we assume that b value remains constant with time (consistent with measurements on subsets of data in Figure 8c) then the estimate above is biased low (the catalog lacks small LFEs when the background tremor amplitude is large) and we may correct by detrending the data and recalculating a power law fit to the resulting normalized moments, as shown in Figures 8c and 8d. The exponent $\beta = 6.05 \pm 0.15$ $b \approx 7.5$ and, as before, the power law fit is significantly better than that for exponential decay.

4.3. Magnitudes in Space

Figure 9 presents the equivalent moment magnitude corresponding to cumulative moment over the 10 ETS events between 2003 and 2013 for each of the 130 templates in our catalog. These magnitudes vary between 3.6 and 4.6 with little obvious spatial pattern, save for a weak tendency for smaller cumulative moments at greater depths which may be due to inter-ETS slip at depth [*Wech and Creager*, 2011].

4.4. Magnitudes in Time

In Figure 10a, we plot magnitude versus Julian day for detections associated with template 002 during the 2003 episode. This template is located in the eastern arm of the region analyzed by *Rubin and Armbruster* [2013] who used integrated square of velocity as a measure for LFE size (see their Figures 5 and 8), and our observations mirror theirs for the period of 3–4 March. This template/episode pair portrays a behavior that is frequently observed across many template/episodes. The inferred main slip front arrival at Julian day 62.3 (3 March, 7:00 A.M.) is marked by low-magnitude events $M_W \sim 1.4$ occurring frequently at brief intervals. The upper envelope of magnitudes increases rapidly to $M_W \sim 2.0$ over the first half day of activity and then levels off. The timing of detections begins to develop more organization at this point (March 4, A.M.) in the form of bursts of LFE activity occurring on a quasi-hourly basis that *Rubin and Armbruster* [2013] identified with small-scale secondary fronts. These bursts vary in maximum amplitude and include one burst between Julian day 63.5 and 63.59 with individual events reaching $M_W = 2.35$. After 5 March (Julian day 64) the bursts become more sporadic with four more occurrences prior to the end of the episode at days 64.6, 68.3, 68.35, and 68.7). As we shall demonstrate in the following section, these later bursts represent more spatially extensive RTRs [*Houston et al.*, 2011]. Approximately 50% of the total moment for most template/episodes is accumulated within the first day of activity during which sensitivity to tidal modulation is low, whereas the remainder comes primarily from the larger discrete bursts (i.e., RTRs) that occur in the following days and possess a stronger sensitivity to tides as reported by *Houston* [2015] and *Royer et al.* [2015]. For some templates/episodes, particularly those for which template locations lie farther downdip, the moment release is more punctuated within a given episode (Figure 10b), unlike their behavior over longer time periods [e.g., *Wech and Creager*, 2011].

4.5. Magnitudes in Space-Time

ETS migration beneath southern Vancouver Island typically proceeds along strike from SE to NW, although other behaviors are also observed [e.g., *Kao et al.*, 2009]. Figure 11 displays LFE activity in along-strike distance versus data plots for episodes in 2005 during which migration was normal (see also 2004 in Figure 12), 2012 during which migration proceeded from NW to SE, and 2013 during which separate primary fronts propagating from the NW and from the SE converged within the study region. LFE occurrences are color-coded with respect to magnitude and reveal that the majority of events exceeding magnitude $M_W \sim 2$ appear as RTRs with along-strike dimensions approaching and occasionally exceeding 40 km, consistent with the observations of *Houston et al.* [2011] and *Thomas et al.* [2013]. A 1 h running summed moment is displayed at the top of the plots and further emphasizes the punctuated moment release within RTRs. Plane-wave fits to RTR fronts

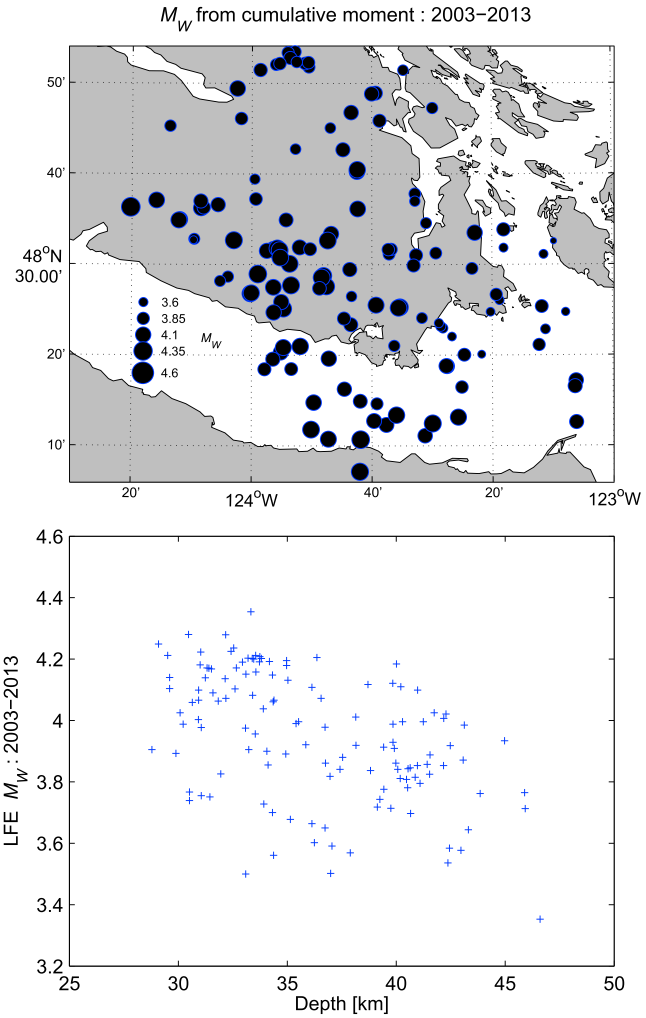

Figure 9. Cumulative moment for ETS episodes between 2003 and 2013 represented as equivalent moment magnitudes for 130 template-families as a function of (top) epicentral location and (bottom) depth.

suggest typical speeds of 10–50 km/h and variable azimuths, although deviations from planarity are likely significant [e.g., *Peng et al.*, 2015]. In the 2013 event, RTRs are strongly generated where the two oppositely vergent fronts collide and propagate back along strike in both directions. In Figure 12 we plot a time distance graphs for 2004 that include all LFEs (top), LFEs restricted to depths above 35 km (middle), and depths below (35 km) (bottom). The RTR signature is significantly better represented for updip events, an observation that holds across all episodes.

4.6. Scaling and Self-Similarity

Most moment-duration scaling studies [e.g., *Prieto et al.*, 2004] are conducted in the frequency domain because direct arrival waveforms are often contaminated by strong secondary phases produced through, e.g., scattering and triplication. This complexity is reflected primarily in the phase spectrum, whereas the amplitude spectrum is left relatively unaffected. Regular earthquakes are typically inferred to exhibit self-similarity [*Kanamori and Anderson*, 1975] that can be expressed in a scaling relation between moment and characteristic duration τ as $M_0 \propto \tau^3$ [e.g., *Houston*, 2001]. Moment-duration scaling for a population of self-similar earthquakes in the frequency domain is manifest through a translation of their amplitude spectra along a ω^{-3} trajectory [e.g., *Prieto et al.*, 2004]. The simplicity of the direct *P* and *S* arrivals on our LFE templates for stations at near epicentral distances allows us to exploit both amplitude and phase information within the time domain (see Figure 14). Earthquake self-similarity will be expressed in time domain waveforms as a scaling in pulse amplitude that is the square of scaling in pulse duration leading once more to the relation $M_0 \propto \tau^3$, since moment is proportional to integrated far-field displacement.

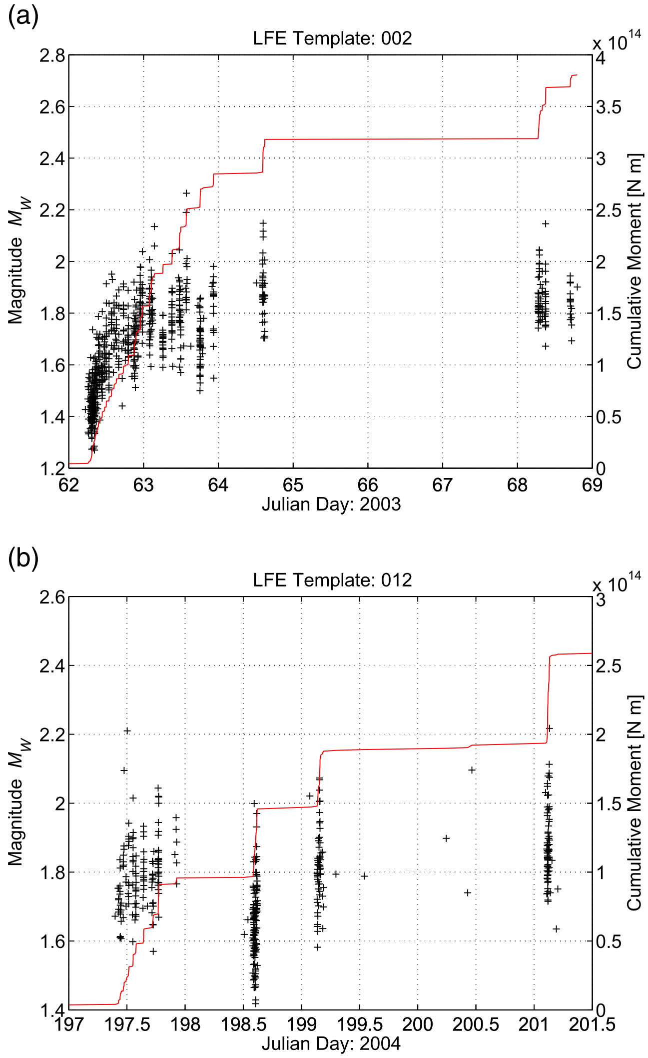

Figure 10. Magnitudes of detections associated with LFE (a) template 002 as a function of Julian day in March 2003 and (b) template 012 in July 2004.

Before proceeding it is worth considering whether LFEs should be characterized by a well-defined duration or corner frequency f_c (note that here we shall define duration as $\tau = 1/f_c$ rather than reciprocal radial frequency). By stacking long-period (0.02–0.05 Hz) seismograms at times when tremor amplitudes were high, *Ide and Yabe* [2014] identified very low frequency (VLF) events in Nankai and argued that there is a continuity of source signals from the tremor (or LFE) band to the VLF band that may extend to still lower frequencies used in geodetic observations. In this context, a well-defined LFE corner frequency might not be expected. In Figure 13, we plot stacks of detections (between 1000 and 2000 in number) of unfiltered particle velocity waveforms for the east component of station TWKB from a random selection of eight templates. Figure 13 (left) displays 1 min traces where some relict microseismic noise is evident; Figure 13 (right) shows a 6 s inset about the main *S* arrival. From visual inspection, the seismograms in Figure 13 possess a dominant frequency near 2 Hz. Hence, we conclude that LFEs are characterized by a well-defined corner frequency and corresponding duration.

4.6.1. Pulse Duration, Instantaneous Frequency, and Duration-Amplitude Scaling

By definition, particle velocity spectra peak at the corner frequency. For example, velocity spectra for the ω-square model [e.g., *Aki*, 1967] exhibit symmetric $\pm\omega^{-1}$ asymptotes intersecting at the nominal corner frequency. Since many high-SNR LFE template waveforms exhibit simple pulses associated with direct arrivals

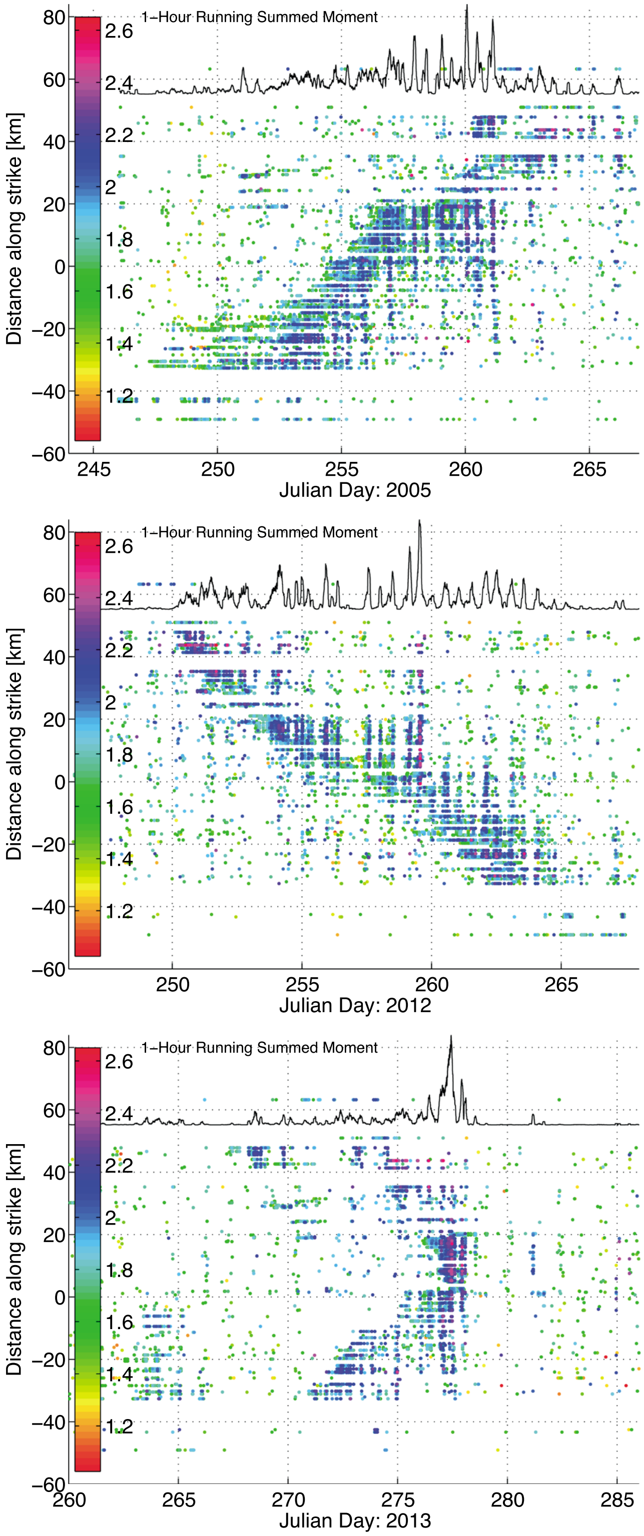

Figure 11. Space-time plots of LFE magnitudes for the (top) 2005, (middle) 2012, and (bottom) 2013 ETS events. One hour running summed moment is plotted at the top of each figure.

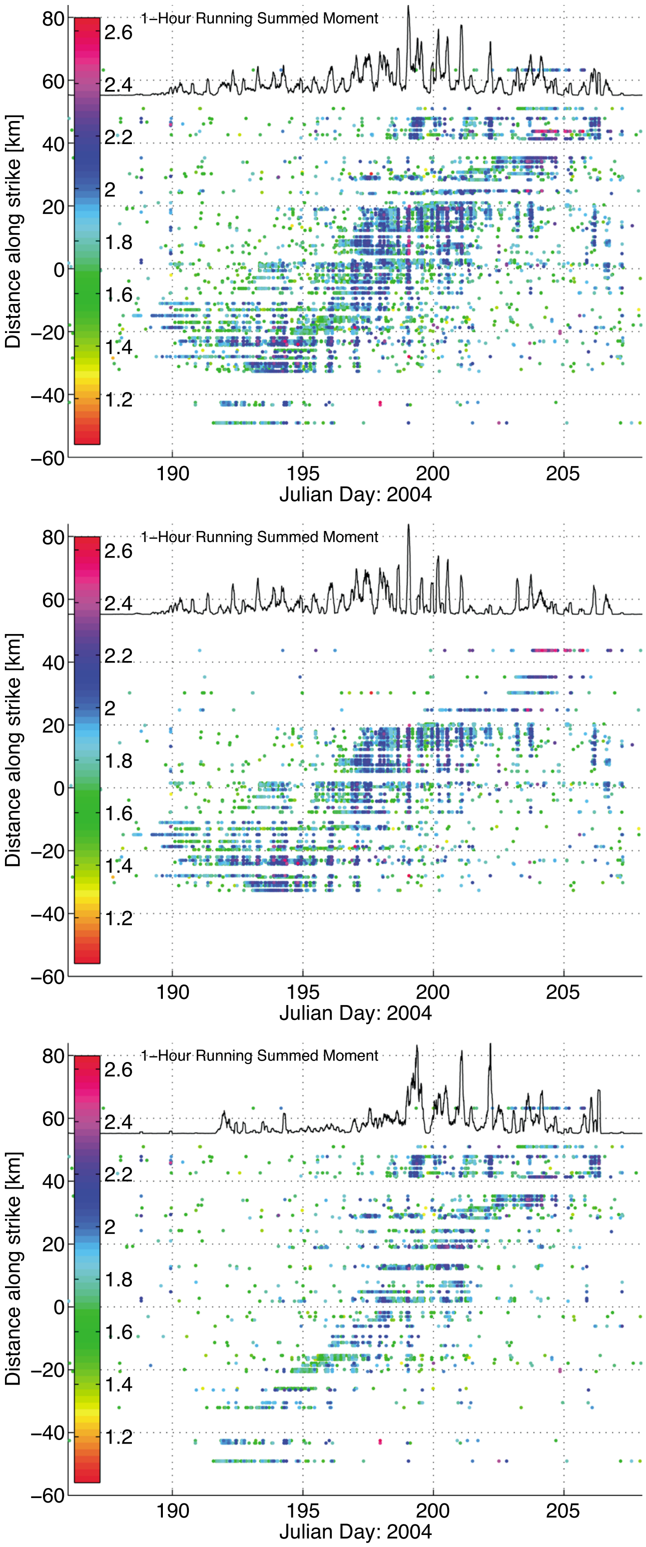

Figure 12. Space-time plots of magnitudes for all (top) LFEs in the 2004 ETS event, (middle) LFEs above 35 km depth in 2004, and (bottom) LFEs below 35 km depth in 2004. One hour running summed moment is plotted at the top of each figure.

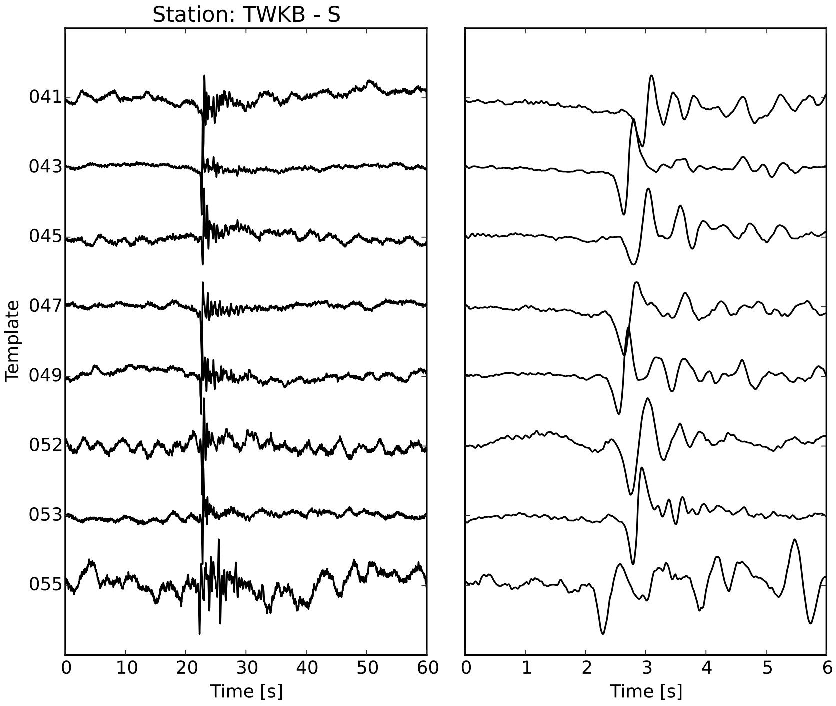

Figure 13. Stacks of unfiltered particle velocity waveforms for the east component of station TWKB and a selection of eight templates. (left) A 60 s window; (right) a 6 s inset about the main *S* arrival. Visual inspection reveals a dominant frequency near 2 Hz.

and are largely devoid of interference from multipathing, we may employ instantaneous frequency $f(t)$ (and its reciprocal) in the measure of corner frequency (and pulse duration) [e.g., *Barnes*, 2007]. This quantity is computed as

$$f(t) = \frac{1}{2\pi}\left[\frac{v(t)\frac{dh(t)}{dt} - h(t)\frac{dv(t)}{dt}}{v^2(t) + h^2(t)}\right], \qquad (12)$$

where $v(t)$ is a given template (particle velocity) waveform and $h(t)$ is its Hilbert transform. Although instantaneous frequency can vary widely over a template trace especially where signal amplitudes (and the denominator in (12)) are low, it is generally well behaved over the time interval corresponding to a high-SNR direct *P* or *S* wave arrival, and we shall employ the mean value in an interval ± 0.05 s about the maximum of $h(t)$ as our corner frequency measure (see Figure 14). Note that $h(t)$ will tend to exhibit a symmetric pulse (versus the generally antisymmetric $v(t)$ pulse) with a duration that is readily visualized.

To examine the relation between moment and pulse duration for LFEs, we isolate all detections within two magnitude ranges: a low-magnitude range between $M_W < 1.5$ and a high-magnitude range $M_W \geq 2.0$. The total detections number 27,925, 23,130 in the respective bins, although detections for individual station-channels within specific templates are not necessarily represented in similar proportions. Moreover, nominal moments and magnitudes (computed as mean and magnitude equivalent to mean, respectively) for the two sets of waveforms vary slightly across template channels according to data availability. For each detection bin, we construct particle velocity templates for each station-channel through averaging (while preserving absolute amplitudes) and for those LFE template and channel combinations that exhibit high similarity. Some filtering is necessary to remove the influence of microseismic noise. Bearing Figure 13 in mind, we apply a conservative, eight-pole, two-pass, 0.3–10 Hz Butterworth band-pass filter to the data to avoid biasing the corner frequency measurement. In addition, we apply splitting corrections to the *S* waveforms to minimize pulse broadening resulting from anisotropy [*Matharu et al.*, 2014], and multichannel-cross-correlation time corrections to individual detections on any given channel to minimize pulse broadening in stacks due to small hypocentral variations among detections. Examples of 60 waveforms for which instantaneous frequency measurements were made are displayed in Figure 15. Note that waveforms corresponding to the lower magnitude bin have been scaled by a factor of 10.

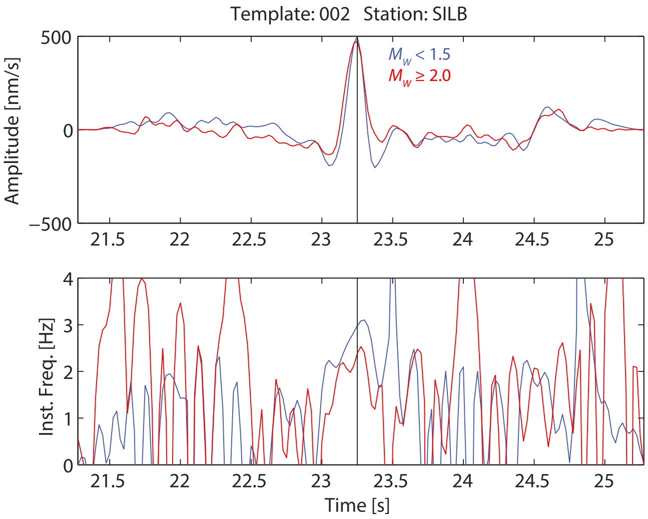

Figure 14. Pulse duration from instantaneous frequency. (top) Hilbert transformed, particle velocity, template *S* waveforms on split- and hypocenter-corrected component of station SILB prepared from mean stack of detections with magnitudes $M_W < 1.5$ (blue) and $M_W \geq 2.0$ (red). Amplitude of the former trace has been scaled by a factor of 10. Mean moments for detections contributing to the two waveforms are $M_0^{(1)} = 1.80 \times 10^{11}$ N m and $M_0^{(2)} = 1.65 \times 10^{12}$ N m, respectively. (bottom) Instantaneous frequency over the same time interval for the corresponding traces. Although this quantity fluctuates, it is well behaved in the vicinity of peak amplitude (vertical black line) providing a time domain estimate of corner frequency and enabling calculation of relative duration $\tau(M_0^J)/\tau(M_0^K) = f(M_0^K)/f(M_0^J) = 2.94\text{Hz}/2.28\text{Hz} = 1.29$.

As mentioned above, consideration of waveforms in the time domain enables us to deliver additional constraint on the nature of magnitude scaling through the availability of phase information. Consider template waveforms for an individual station-channel extracted from two bins with nominal moments M_0^K and M_0^J representing a given asperity on the plate boundary (see Figure 16). Denote the ratio of their pulse durations $\tau^J/\tau^K = b_r$ (computed from instantaneous frequency as f^K/f^J) and the ratio of their amplitudes as $A^J/A^K = b_r b_D$. Here we assume that rupture velocity V_R is independent of moment (consistent with self-similarity) and so associate pulse duration ratio τ^J/τ^K with the ratio b_r of rupture dimension for the corresponding nominal faults (Figure 16). Although source rise-time contributes to the pulse duration, its effect

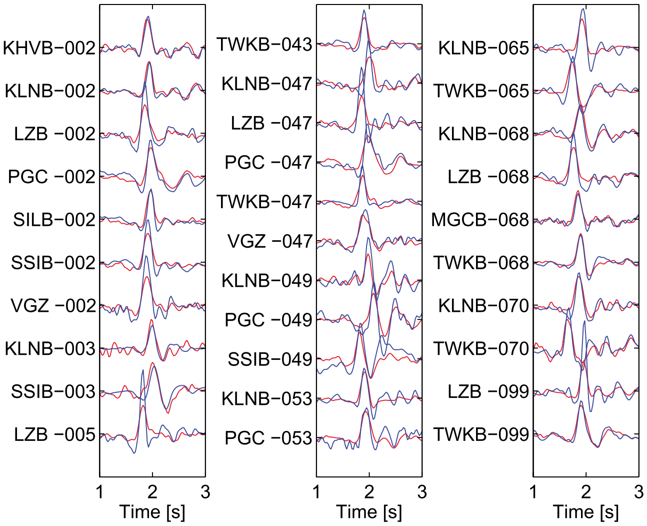

Figure 15. Example (Hilbert-transformed, particle velocity) template *S* waveforms from mean stacks of detections for bins with magnitudes $M_W < 1.5$ (blue) and $M_W \geq 2.0$ (red). Blue traces have been scaled by a factor of 10 but relative scaling for individual channels is otherwise maintained. Waveforms have been corrected for splitting and for time shifts associated with hypocentral variations for individual detections. Station template identification is indicated at left. Note similarity in dominant frequency for and across individual template channels.

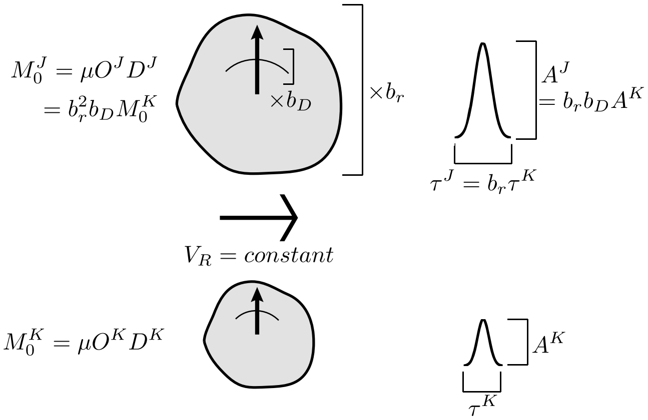

Figure 16. Cartoon illustrating scaling relations between asperity dimensions and particle displacement waveform attributes for two asperities registering moments M_0^J and M_0^K with areas O^J, O^K and slip displacements D^J, D^K under the assumption that rupture velocity V_R is constant, after *Prieto et al.* [2004]. Displacement vector associated with slip is shown as vertical arrow, whereas scaling in rupture dimension and slip are denoted b_r and b_D, respectively. The corresponding pulse amplitudes and durations are denoted A^J, A^K and τ^J, τ^K, respectively.

for regular earthquakes is thought to be small (~ 10% [e.g., *Heaton*, 1990]) and will be ignored here. Likewise, b_D is the ratio of slips on the two nominal faults. LFE self-similarity would imply that these scaling parameters are equal, that is $b_r = b_D$ [*Prieto et al.*, 2004]. A cursory examination of Figure 14 suggests that self-similarity is not honored. The ratio of mean amplitudes is $A^J/A^K = b_r b_D = 474.4\text{nms}^{-1}/50.0\text{nms}^{-1} = 9.49$, whereas the pulse duration ratio is $f^K/f^J = b_r = 2.94\,\text{Hz}/2.28\,\text{Hz} = 1.29$. These values are typical for template waveforms extracted from the low- and high-magnitude bins (see Figure 17). Accordingly, we recover a value of $b_D = 7.36$, the ratio of slip for the events with nominal moments $M_0^J = 1.65{\times}10^{12}\text{Nm}$ and $M_0^K = 1.80{\times}10^{11}\text{Nm}$. That is, larger moment events appear to be primarily the result of increased slip, with increased fault area playing a more minor role than expected for LFE self-similarity. Similar conclusions were drawn by *Harrington and Brodsky* [2009] for an isolated family of repeating earthquakes on the San Andreas Fault near Parkfield.

Before proceeding, we consider a possible source of contamination. Our inclusion of an attenuation correction in (4) accounts only for amplitude attenuation, and the LFE magnitude distribution prevents us from attempting an empirical Green's function deconvolution [e.g., *Hough*, 1997] to remove dispersion due to attenuation. It is conceivable that strong along-path attenuation might produce pulse broadening similar to that in Figure 17 if LFE corner frequencies for the range of nominal magnitudes $M_W = 1.0–2.6$ were markedly higher than the observation pass band of 1–8 Hz. We consider this possibility unlikely since (i) seismograms of intraslab events with overlapping and longer paths retain significant energy to frequencies of 40 Hz or more and (ii) attenuation modeling of tremor and intraslab events in Cascadia and other subduction zones has shown that the latter are more severely attenuated than the former due to their additional transit through a low-Q layer at the top of the subducting plate [*Yabe et al.*, 2014].

4.6.2. Fault Dimensions and Stress Drop

The pulse broadening observations made in the previous section can be used, along with catalog moments $M_0^J = \mu O^J D^J$, to constrain absolute estimates (versus ratios) of fault slip D^J, fault area O^J, and stress drop $\Delta\sigma^J (= C\mu D^J/\sqrt{O^J}$ where C is a geometrical constant of order (1) for an individual LFE. Motivated by the relation

$$\frac{M_0^J}{M_0^K} = \frac{O^J D^J}{O^K D^K} = b_r^2 b_D, \tag{13}$$

we can pose two regression problems: one where the data are slip ratios $b_D = D^J/D^K = \frac{A^J f^J}{A^K f^K}$ and both amplitude and duration measurements are employed using nominal moments M_0^J, M_0^K corresponding to the two sets of bins ($M_W < 1.5$ and $M_W \geq 2.0$) for a given family and station-channel template waveform and a second where the data are $b_r = \sqrt{O^J/O^K} = \frac{f^K}{f^J}$ and only the duration measurements enter. We parameterize these ratios as

$$b_D(M_0^J/M_0^K) = \left(\frac{M_0^J}{M_0^K}\right)^{\gamma}, \qquad b_r(M_0^J/M_0^K) = \left(\frac{M_0^J}{M_0^K}\right)^{(1-\gamma)/2}, \tag{14}$$

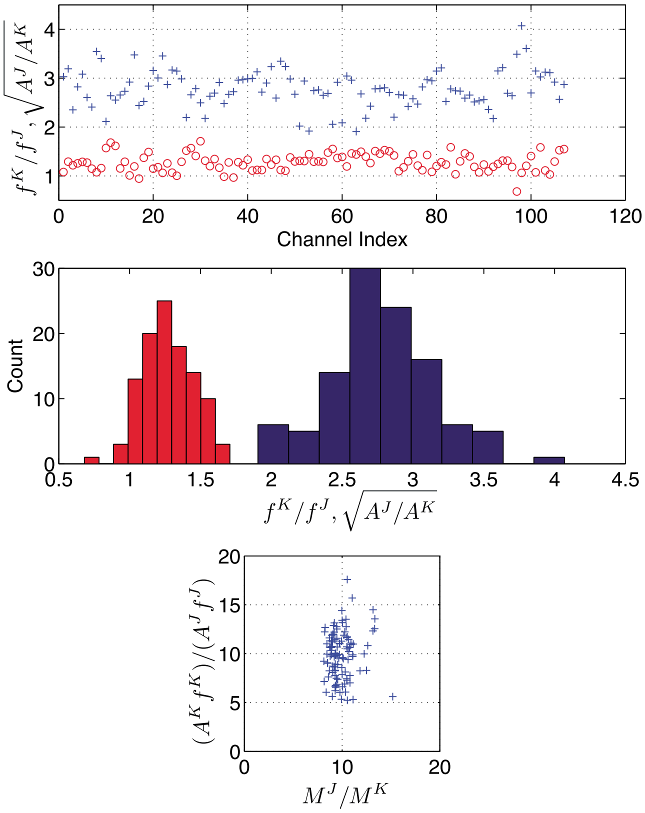

Figure 17. Data used to determine scaling coefficient $\gamma = 0.79$. (top) Values of $f^K/f^J = b_r$ (red circles) and $\sqrt{A^J/A^K} = \sqrt{b_r b_D}$ (blue crosses) measured from template waveforms generated from end-member magnitude bins ($M_W < 1.5$, $M_W \geq 2.0$, respectively). (middle) Corresponding histograms. (bottom) The ratio $[A^J f^K]/A^K f^J]$ versus M_0^J/M_0^K. Both of these quantities should equate to $b_r^2 b_D$. Their values cluster around the point (10,10) and so display internal consistency.

where γ is an exponent to be determined, and we have explicitly indicated the dependence of b_D, b_r on moment ratio M_0^J/M_0^K. By taking logarithms, we transform both systems to linear and solve for γ, using the 110 station-channel pairs J, K whose template waveforms exhibit correlation coefficients satisfying conditions similar to those applied in selection of candidate channels for magnitude determination (see section 2):

$$\gamma = \log\left(b_D\right)/\log\left(\frac{M_0^J}{M_0^K}\right), \qquad \gamma = 1 - 2\log\left(b_r\right)/\log\left(\frac{M_0^J}{M_0^K}\right). \tag{15}$$

The raw measurements are shown in Figure 17 (top and middle) and display values (mean 1.28) of $f^K/f^J = \tau^J/\tau^K$ that lie systematically below those of $\sqrt{A^J/A^K}$ (mean 2.78). As a consistency check, we plot $\frac{A^J f^K}{A^K f^J}$ versus M_0^J/M_0^K in Figure 17 (bottom). In principle, both quantities should equate to $b_r^2 b_D$, and so form a line with slope of 1 in the vicinity of the value 10, based on the nominal moments for the chosen magnitude bins across the families considered. Although there is greater spread in $\frac{A^J f^K}{A^K f^J}$ values due to the greater variance in single-channel measurements, they cluster about the coordinate (10,10) and so are consistent with the corresponding moment ratios.

The solutions to (15), $\gamma = 0.78, 0.80$, lie well above the value $\gamma = 1/3$ expected for self-similarity and quantify the dominance of displacement in controlling moment. Given $\gamma = 0.79$, it follows that scaling in fault dimension and stress drop can be written as

$$\sqrt{\frac{O^J}{O^K}} = \left(\frac{M_0^J}{M_0^K}\right)^{0.105}, \qquad \frac{\Delta\sigma^J}{\Delta\sigma^K} = \left(\frac{M_0^J}{M_0^K}\right)^{0.685}, \tag{16}$$

respectively.

In principle, we might use the expression for slip in (14) to estimate absolute fault dimensions and stress drop by assuming a known total slip on each LFE source accumulated during either of the two ETS episodes (2004 and 2005) for which our LFE catalogs are most complete. For updip LFE families that experience little or no activity during inter-ETS periods [*Wech and Creager*, 2011] we expect this total slip to be a significant fraction of the relative plate motion rate times the recurrence interval, $\sim$ 4 cm (this is consistent with the geodetic inversions of *Schmidt and Gao* [2010]). Taking this total slip to be 4 cm, we further assume for illustrative purposes that (1) our catalog is complete, (2) each LFE template represents a single physical source, and (3) the entire moment released within the confines of an LFE asperity is manifest within the tremor band (although it is certainly possible that some slip occurs at still lower frequencies, this assumption is not inconsistent with Figure 13 that indicates a lack of continuum of slip at frequencies below the tremor band). Then, the total slip is the sum of the slip produced in all LFE detections for a given template and year, which we relate to the slip D^R for a reference moment M_0^R as

$$\sum_J D^J = \sum_J b_D(M_0^J/M_0^R)D^R = 0.04\ \text{m}. \tag{17}$$

Inserting the form in (14) for $b_D(M_0^J/M_0^R)$ yields

$$D^R = \frac{0.04\ \text{m}}{\sum_J \left(\frac{M_0^J}{M_0^R}\right)^{0.79}}. \tag{18}$$

As an example, we consider detections in 2004 for template 001 with location identified in Figure 1. Taking a reference moment of $M_0^R = 1.26 \times 10^{12}$ N m corresponding to magnitude $M_W = 2$, we find a slip of $D^R \sim 1.23 \times 10^{-4}$ m, characteristic fault dimension $\sqrt{O^R} \sim 585$ m, and stress drop $\Delta\sigma^R = 15.3$ kPa (assuming a shear modulus $\mu = 30$ GPa and circular fault). Although these values appear reasonable in light of previous work [e.g., *Rubin*, 2008; *Sweet et al.*, 2014], the assumptions listed above are highly questionable for a number of reasons. We consider this issue further in the following section.

5. Discussion and Concluding Remarks

We have assembled an LFE magnitude catalog for southern Vancouver Island that encompasses 10 ETS episodes between 2002 and 2013. Spatiotemporal patterns reported in previous studies involving more qualitative analysis of amplitudes [*Rubin and Armbruster*, 2013; *Thomas et al.*, 2013] are corroborated. Perhaps the most interesting results from this study center on observations that indicate a limitation on the spatial extent of asperities that generate LFEs. First, the maximum magnitude $M_W \sim 2.6$ lies well below that of regular earthquakes for an equivalent catalog size and implies a restriction on fault dimensions. The magnitude-frequency distribution is also unusual. A previous study [*Sweet et al.*, 2014] of a single LFE family in Washington state argued that LFE magnitudes were better explained by an exponential distribution than by a power law (i.e., Gutenberg-Richter) relation, consistent with earlier work on tremor amplitude and duration in Nankaii by *Watanabe et al.* [2007]. The latter study noted that an exponential distribution is characteristic of a scale-bound source process rather than a scale-invariant one. Although southern Vancouver Island magnitudes are better fit by power law distributions, the observed b values $\gtrsim 5$ (Figure 8) are like, those of *Sweet et al.* [2014], much larger than b values cited for regular seismicity that typically range between 0.7 and 1.5 [e.g., *Scholz*, 2015]. The paucity of larger events implied by the large b values could conceivably be influenced by reduced similarity between template waveforms (constructed from large numbers of small-magnitude detections) and waveforms of larger LFEs, resulting in reduced detections and distortion of the magnitude-frequency distribution. However, we regard this scenario as unlikely given that larger LFEs should be preferentially identified as starting templates in the template construction process [*Savard and Bostock*, 2015]. In addition, LFE detections based on correlating the same time window at different stations [e.g., *Rubin and Armbruster*, 2013], rather than different time windows at the same station, are not susceptible to this potential bias. Examining all the “simple” detections (those dominated by a single main arrival) identified by such a cross-channel correlation scheme, when applied to a few of the LFE templates in this study, shows zero anomalously wide large-magnitude events or anomalously narrow small-magnitude events.

Given the superior fit of power law over exponential distributions shown Figure 8, we may consider the interpretation that b values vary inversely with differential stress [*Scholz*, 1968; *Bachmann et al.*, 2012], with high-stress environments producing larger proportions of high-magnitude events (low *b* values) than low-stress environments (high *b* values). This relation is qualitatively consistent with the observation that slow-slip phenomena including low-frequency earthquakes are associated with low effective stress [e.g., *Rubinstein et al.*, 2008] through elevated pore fluid pressures [*Audet et al.*, 2009]. Nonetheless, LFE *b* values are difficult to reconcile quantitatively, yielding, for example, negative values of differential stress when applied to regression formulae derived from regular earthquakes [*Scholz*, 2015], thereby implying fundamentally different controls on their generation.

The most revealing constraints on LFE moment scaling arise from analysis of LFE pulse durations and amplitudes as manifest in template waveforms constructed from LFE detections at the upper and lower limits of the magnitude distribution. By assuming that pulse duration is proportional to fault dimension (as is routinely done in studies of source directivity), we can isolate the effects of moment scaling in fault area from scaling in displacement. The scaling of LFE moment with duration is weak. For example, to achieve a moment ratio of 10 (comparable to moment ratios for the two magnitude bins considered in the previous section and in, e.g., Figure 14), requires a scaling in duration to the power $\sim$ 9–10, that is $(1.27)^{9.7} \approx 10.0$. If rupture velocity is independent of moment, this observation requires that fault dimensions are effectively limited and that most of the variation in moment is due to variable slip, implying variable stress drop. By further assuming a total slip of 4.0 cm per ETS episode for updip families and that all detections rupture a common region of the fault surface, this scaling can be employed to estimate characteristic fault dimension, slip, and stress drop for an LFE of given magnitude as well as rupture velocity, as reported in the previous section. Correction for anticipated levels of catalog incompleteness using the β values recovered from power law modeling and modest minimum magnitudes of $\check{M}_W > 1.0$ results in millions of missed events and estimates of fault dimensions (tens of kilometers) and stress drop (10^{-2} Pa) that stray considerably from plausible values. Larger β, implied in Figure 8d, and/or smaller $\check{M}_W$ further exacerbate the discrepancy.

A reconciliation can be achieved by relaxing the assumption that each detection represents rupture on a common region of fault. If *n* independently slipping sources are present within the template footprint (i.e., the area that gives rise to detections for a given template), then our estimates will change as $D^R_{n>1} = nD^R_{n=1}$, $\sqrt{O^R_{n>1}} = \sqrt{O^R_{n=1}/n}$, and $\Delta\sigma^R_{n>1} = n^{3/2}\Delta\sigma^R_{n=1}$. Some constraint on the true limit $\check{M}_W$ of the distribution may be delivered by the size of template footprint which, from template waveform correlations, does not exceed $\sim$ 4 km in diameter. Returning to the example of template 001, we find that a catalog completeness correction down to $\check{M}_W = 1.60$ (using $\beta = 5.58$ from the power law fit for this particular family) increases the detection count from 564 to 37069 and will produce $\sqrt{O^R_{n=1}} \approx 4.0$ km. A value of $n = 45$ then suffices to return estimates of $D^R_{n>1}$, $\sqrt{O^R_{n>1}}$, and $\Delta\sigma^R_{n>1}$ to the values cited in section 4.6.2, while filling the template footprint with sources. Further revision of $\check{M}_W, n$ may be required to ensure consistency between typical pulse durations of $\sim$ 0.5 s and plausible rupture velocities, and the requirement of some degree of isolation between seismogenic patches such that larger LFEs remain spatially confined (as the moment-duration scaling analysis indicates) without rupturing into adjacent source areas, given the source densities implied. At present, our knowledge of the proper form of LFE magnitude-frequency relation is poorly constrained. Power law descriptions of natural processes are valid over finite ranges and it is likely, given the large values of β, that the LFE moment range for power law applicability is significantly reduced relative to that for regular earthquakes and that the generative mechanism is distinct. In particular, the correlation in Figure 8b invites speculation as to whether the LFE magnitude-frequency relation is directly governed by the local slow slip event (SSE) moment rate; that is, that larger-magnitude LFEs are produced during periods of faster slip. Such behavior would distinguish LFEs from regular repeating earthquakes, where faster fault slip leads to more frequent occurrence of similar-sized events [e.g., *Schaff et al.*, 1998].

An alternative mechanism for accommodating the observed LFE moment-duration behavior is through a moment-dependent rupture speed, that is, that larger LFEs involving larger fault areas exhibit greater rupture speeds such that LFE duration remains approximately constant. In that context, a maximum fault dimension is still implied and set by shear velocity as an upper limit on rupture speed. For example, if the rupture speed of the largest observed ($M_W = 2.6$) LFE equals 3000 m/s, a characteristic duration of 0.5 s would correspond to a fault dimension of 1.5 km. Lower shear velocities implied by structural studies [*Audet et al.*, 2009] would produce correspondingly smaller dimensions if such velocities are representative for LFE source regions. Note that a rupture velocity proportional to fault dimension runs contrary to the observation that larger SSEs slip more slowly than smaller ones [e.g., *Ide et al.*, 2007; *Gao et al.*, 2012]. Furthermore, as a physical mechanism capable of producing a moment-proportional rupture speed is not immediately evident [e.g., *Harrington and Brodsky*, 2009], we favor the interpretation of an approximately constant LFE asperity dimension.

The weak dependence of moment on duration is apparently at odds with the slow earthquake scaling law proposed by *Ide et al.* [2007] in which LFEs and SSEs are considered as end members. This model posits that slow earthquake moment scales with the first power of duration in contrast to regular earthquakes that scale with duration cubed as required for self-similarity. Accordingly, we might expect that two LFEs that differ in moment by a factor of 10 would display a scaling in duration of $\sim$ 2.2, in contrast to the mean value of 1.28 observed here. Indeed, whereas both constant stress drop and constant slip models have been proposed for SSEs within the context of a linear moment-duration scaling [*Ide et al.*, 2007] and regular earthquakes generally conform with self-similarity [*Kanamori and Anderson*, 1975], it appears that LFEs are best represented by a constant fault dimension model. We suggest that LFEs and SSEs are fundamentally distinct and might be expected to obey different scaling relations. SSEs are areally extensive ($\sqrt{O} \sim$ 100 km) and their behavior is governed by average fault properties over comparable dimensions. In particular, the plate boundary region within the transition zone over these scale lengths is known to possess anomalously low shear strength [e.g., *Audet et al.*, 2009]. Whether these average properties apply locally over the areas ($\sqrt{O} <\sim$ 1 km) where LFE rupture occurs is unclear. However, the very existence of LFEs, their persistance in time and their stationarity in space suggests that structural heterogeneity, perhaps related to low-permeability pockets of upper oceanic crust impervious to hydrothermal circulation [*Bostock*, 2013] or localized breaches of the plate boundary seal [*Audet et al.*, 2009], is a fundamental control.

Acknowledgments
We gratefully acknowledge the IRIS Data Management Center and the Geological Survey of Canada for allowing access to the seismological waveform data employed in this study. Special thanks to Tim Côté at the G.S.C. for recovering data from portable experiments in 2004 and 2005. We thank Robert Nadeau, Zhigang Peng, and David Shelly for useful discussions on an early presentation of this work, and constructive reviews from Satoshi Ide and an anonymous referee. Power law modeling was undertaken with Jeff Alstott's Python power law package. This study was supported by NSERC Discovery grant RGPIN 138004 to M.G.B. and NSF EAR-PF Award 1249775 to A.M.T. and NSF award EAR 1344948 to A.M.R.

References

Aguiar, A. C., T. I. Melbourne, and C. W. Scrivner (2009), Moment release rate of Cascadia tremor constrained by GPS, *J. Geophys. Res.*, *114*, B00A05, doi:10.1029/2008JB005909.
Aki, K. (1967), Scaling law of seismic spectrum, *J. Geophys. Res.*, *72*, 1217–1231.
Alstott, J., E. Bullmore, and D. Plenz (2014), Powerlaw: A Python package for analysis of heavy-tailed distributions, *PLoS ONE*, *9*, e85777, doi:10.1371/journal.pone.0085777.
Andrews, D. J. (1986), Objective determination of source parameters and similarity of earthquakes of different size, in *Earthquake Source Mechanics, Geophys. Monogr. Ser.*, vol. 37, edited by S. Das, J. Boatwright, and C. H. Scholz, pp. 259–267, AGU, Washington, D. C.
Armbruster, J. G., W.-Y. Kim, and A. M. Rubin (2014), Accurate tremor locations from coherent S and P waves, *J. Geophys. Res. Solid Earth*, *119*, 5000–5013, doi:10.1002/2014JB011133.
Audet, P., M. G. Bostock, N. I. Christensen, and S. M. Peacock (2009), Seismic evidence for overpressured subducted oceanic crust and megathrust fault sealing, *Nature*, *457*, 76–78.
Bachmann, C. E., S. Wiemer, B. P. Goertz-Allmann, and J. Woessner (2012), Influence of pore-pressure on the event-size distribution of induced earthquakes, *Geophys. Res. Lett.*, *39*, L09302, doi:10.1029/2012GL051480.
Balfour, N. J., J. F. Cassidy, and S. E. Dosso (2011), Crustal anisotropy in the forearc of the northern Cascadia subduction zone, British Columbia, *Geophys. J. Int.*, *188*, 165–176, doi:10.1111/j.1365-246X.2011.05231.x.
Baltay, A. S., and G. C. Beroza (2013), Ground-motion prediction from tremor, *Geophys. Res. Lett.*, *40*, 6340–6345, doi:10.1002/2013GL058506.
Barnes, A. E. (2007), A tutorial on complex seismic trace analysis, *Geophysics*, *72*, W33–W43.
Bostock, M. G. (2013), The Moho in subduction zones, *Tectonophysics*, *609*, 547–557.
Bostock, M. G., A. A. Royer, E. H. Hearn, and S. M. Peacock (2012), Low frequency earthquakes below southern Vancouver Island, *Geochem. Geophys. Geosyst.*, *13*, Q11007, doi:10.1029/2012GC004391.
Brudzinski, M. R., and R. M. Allen (2007), Segmentation in episodic tremor and slip all along Cascaida, *Geology*, *35*, 907–910.
Bungum, H., and E. S. Husebye (1971), Errors in time delay measurements, *Pure Appl. Geophys.*, *91*, 56–70.
Chapman, C. H. (2004), *Fundamentals of Seismic Wave Propagation*, Cambridge Univ. Press, Cambridge.
Clauset, A., C. R. Shalizi, and M. E. J. Newman (2009), Power-law distributions in empirical data, *SIAM Rev.*, *51*, 661–703, doi:10.1137/070710111.
Dragert, H., K. Wang, and T. S. James (2001), A silent slip event on the deeper Cascadia subduction interface, *Science*, *292*, 1525–1528.
Gao, H., D. A. Schmidt, and R. J. Weldon II (2012), Scaling relationships of source parameters for slow slip events, *Bull. Seismol. Soc. Am.*, *102*, 352–360.
Ghosh, A., J. E. Vidale, and K. C. Creager (2012), Tremor asperities in the transition zone control evolution of slow earthquakes, *J. Geophys. Res.*, *117*, B10301, doi:10.1029/2012JB009249.
Harrington, R. M., and E. E. Brodsky (2009), Source duration scales with magnitude differently for earthquakes on the San Andreas Fault and on secondary faults in Parkfield, California, *Bull. Seismol. Soc. Am.*, *99*, 2323–2334.
Heaton, T. H. (1990), Evidence for and implications of self-healing pulses of slip in earthquake rupture, *Phys. Earth Planet. Inter.*, *64*, 1–20.
Hough, S. E. (1997), Empirical Green's function analysis: Taking the next step, *J. Geophys. Res.*, *102*, 5369–5384.
Houston, H. (2001), Influence of depth, focal mechanism, and tectonic setting on the shape and duration of earthquake source time functions, *J. Geophys. Res.*, *106*(B6), 11,137–11,150, doi:10.1029/2000JB900468.
Houston, H. (2015), Low friction and fault weakening revealed by rising sensitivity of tremor to tidal stress, *Nat. Geosci.*, *8*, 409–415, doi:10.1038/ngeo2419.
Houston, H., B. G. Delbridge, A. G. Wech, and K. C. Creager (2011), Rapid tremor reversals in Cascadia generated by a weakened plate interface, *Nat. Geosci.*, *4*, 404–409, doi:10.1038/ngeo1157.
Ide, S. (2010), Striations, duration, migration and tidal response in deep tremor, *Nature*, *466*, 356–359, doi:10.1038/nature09251.
Ide, S., and S. Yabe (2014), Universality of slow earthquakes in the very low frequency band, *Geophys. Res. Lett.*, *41*, 2786–2793, doi:10.1002/2014GL059712.

Ide, S., G. C. Beroza, D. R. Shelly, and T. Uchide (2007), A scaling law for slow earthquakes, *Nature*, *447*, 76–79, doi:10.1038/nature05780.

Kanamori, H., and D. L. Anderson (1975), Theoretical basis of some empirical relations in seismology, *Bull. Seismol. Soc. Am.*, *65*, 1073–1095.

Kao, H., S.-J. Shan, H. Dragert, G. Rogers, J. F. Cassidy, and K. Ramachandran (2005), A wide depth distribution of seismic tremors along the northern Cascadia margin, *Nature*, *436*, 841–844.

Kao, H., S.-J. Shan, H. Dragert, and G. Rogers (2009), Northern Cascadia episodic tremor and slip: A decade of tremor observations from 1997 to 2007, *J. Geophys. Res.*, *114*, B00A12, doi:10.1029/2008JB006046.

Kao, H., K. Wang, H. Dragert, J. Y. Kao, and G. Rogers (2010), Estimating seismic moment magnitude (Mw) of tremor bursts in northern Cascadia: Implications for the seismic efficiency of episodic tremor and slip, *Geophys. Res. Lett.*, *37*, L19306, doi:10.1029/2010GL044927.

Kennett, B. L. N. (1991), The removal of free surface interactions from three-component seismograms, *Geophys. J. Int.*, *104*, 153–163.

Matharu, G., M. G. Bostock, N. I. Christensen, and J. Tromp (2014), Crustal anisotropy in a subduction zone forearc: Northern Cascadia, *J. Geophys. Res. Solid Earth*, *119*, 7058–7078, doi:10.1002/2014JB011321.

Nicholson, T., M. G. Bostock, and J. F. Cassidy (2005), New constraints on subduction zone structure in northern Cascadia, *Geophys. J. Int.*, *161*, 849–859.

Obara, K. (2002), Nonvolcanic deep tremor associated with subduction in southwest Japan, *Science*, *296*, 1679–1681.

Obara, K., and S. Sekine (2009), Characteristic activity and migration of episodic tremor and slow-slip events in central Japan, *Earth Planets Space*, *61*, 853–862.

Peng, Y., A. M. Rubin, M. G. Bostock, and J. G. Armbruster (2015), High-resolution imaging of rapid tremor migrations beneath southern Vancouver Island using cross-station cross correlations, *J. Geophys. Res. Solid Earth*, *120*, 4317–4332, doi:10.1002/2015JB011892.

Prieto, G. A., P. M. Shearer, F. L. Vernon, and D. Kilb (2004), Earthquake source scaling and self-similarity estimation from stacking of P and S spectra, *J. Geophys. Res.*, *109*, B08310, doi:10.1029/2004JB003084.

Ramachandran, K., S. E. Dosso, G. D. Spence, R. D. Hyndman, and T. M. Brocher (2005), Forearc structure beneath southwestern British Columbia: A three-dimensional tomographic velocity model, *J. Geophys. Res.*, *110*, B02303, doi:10.1029/2004JB003258.

Rogers, G., and H. Dragert (2003), Episodic tremor and slip on the Cascadia subduction zone: The chatter of silent slip, *Science*, *300*, 1942–1943.

Royer, A. A., and M. G. Bostock (2013), A comparative study of low frequency earthquake templates in northern Cascadia, *Earth Planet. Sci. Lett.*, *402*, 247–256.

Royer, A. A., A. M. Thomas, and M. G. Bostock (2015), Tidal modulation and triggering of low frequency earthquakes in northern Cascadia, *J. Geophys. Res. Solid Earth*, *120*, 384–405, doi:10.1002/2014JB011430.

Rubin, A. M. (2008), Episodic slow slip events and rate-and-state friction, *J. Geophys. Res.*, *113*, B11414, doi:10.1029/2008JB005642.

Rubin, A. M., and J. G. Armbruster (2013), Imaging slow slip fronts in Cascadia with high precision cross-station tremor locations, *Geochem. Geophys. Geosyst.*, *14*, 5371–5392, doi:10.1002/2013GC005031.

Rubinstein, J. L., M. La Rocca, J. E. Vidale, K. C. Creager, and A. G. Wech (2008), Tidal modulation of non-volcanic tremor, *Science*, *319*, 186–189.

Savard, G., and M. G. Bostock (2015), Detection and location of low-frequency earthquakes using cross-station correlation, *Bull. Seismol. Soc. Am.*, *105*, 2128–2142, doi:10.1785/0120140301.

Scales, J. A., and A. Gersztenkorn (1988), Robust methods in inverse theory, *Inverse Prob.*, *4*, 1071–1091.

Schaff, D. P., G. C. Beroza, and B. E. Shaw (1998), Postseismic response of repeating aftershocks, *Geophys. Res. Lett.*, *25*, 4549–4552.

Schmidt, D. A., and H. Gao (2010), Source parameters and time-dependent slip distributions of slow slip events on the Cascadia subduction zone from 1998 to 2008, *J. Geophys. Res.*, *115*, B00A18, doi:10.1029/2008JB006045.

Scholz, C. H. (1968), The frequency-magnitude relation of microfracturing in rock and its relation to earthquakes, *Bull. Seismol. Soc. Am.*, *58*, 399–415.

Scholz, C. H. (2015), On the stress dependence of the earthquake b value, *Geophys. Res. Lett.*, *42*, 1399–1402, doi:10.1002/2014GL062863.

Shelly, D. R., G. C. Beroza, S. Ide, and S. Nakamulae (2006), Low-frequency earthquakes in Shikoku, Japan and their relationship to episodic tremor and slip, *Nature*, *442*, 188–191, doi:10.1038/nature04931.

Shelly, D. R., G. C. Beroza, and S. Ide (2007), Complex evolution of transient slip derived from precise tremor locations in western Shikoku, Japan, *Geochem. Geophys. Geosyst.*, *8*, Q10014, doi:10.1029/2007GC001640.

Sweet, J. R., K. C. Creager, and H. Houston (2014), A family of repeating low-frequency earthquakes at the downdip edge of tremor and slip, *Geochem. Geophys. Geosyst.*, *15*, 3713–3721, doi:10.1002/2014GC005449.

Thomas, T. W., J. E. Vidale, H. Houston, K. C. Creager, J. R. Sweet, and A. Ghosh (2013), Evidence for tidal triggering of high-amplitude rapid tremor reversals and tremor streaks in northern Cascadia, *Geophys. Res. Lett.*, *40*, 4254–4259, doi:10.1002/grl.50832.

Watanabe, T., Y. Hiramatsu, and K. Obara (2007), Scaling relationship between the duration and the amplitude of non volcanic deep low frequency tremors, *Geophys. Res. Lett.*, *34*, L07305, doi:10.1029/2007GL029391.

Wech, A. G., and N. M. Bartlow (2014), Slip rate and tremor genesis in Cascadia, *Geophys. Res. Lett.*, *41*, 392–398, doi:10.1002/2013GL058607.

Wech, A. G., and K. C. Creager (2011), A continuuum of stress, strength and slip in the Cascadia subduction zone, *Nat. Geosci.*, *4*, 624–628.

Wech, A. G., K. C. Creager, H. Houston, and J. E. Vidale (2010), An earthquake like magnitude frequency distribution of slow slip in northern Cascadia, *Geophys. Res. Lett.*, *37*, L22310, doi:10.1029/2010GL044881.

Yabe, S., A. S. Baltay, S. Ide, and G. C. Beroza (2014), Seismic-wave attenuation determined from tectonic tremor in multiple subduction zones, *Bull. Seismol. Soc. Am.*, *104*, 2043–2059.

Zhao, D. P., K. L. Wang, G. C. Rogers, and S. M. Peacock (2001), Tomographic image of low P velocity anomalies above slab in northern Cascadia subduction zone, *Earth Planets Space*, *53*, 285–293.